



DR JACK TUSZYNSKI (Orcid ID : 0000-0001-9976-0429)

Article type : Research Article

Computer-Aided Drug Design of Small Molecule Inhibitors of the ERCC1-XPF Protein-Protein Interaction

Running title: *Computer-aided drug design of ERCC1-XPF inhibitors*

Francesco Gentile^{1,1#}, Ahmed H. Elmenoufy^{2,3#}, Gloria Ciniero^{4,5}, David Jay⁶, Feridoun Karimi-Busheri⁶, Khaled H. Barakat⁷, Michael Weinfeld^{6,8}, Frederick G. West^{2,8} and Jack A. Tuszynski^{1,4,6*}

¹Department of Physics, University of Alberta, Edmonton, AB T6G 2E1, Canada

²Department of Chemistry, University of Alberta, Edmonton, AB T6G 2G2, Canada

³Department of Pharmaceutical Chemistry, College of Pharmacy, Misr University for Science and Technology, P.O. Box: 77, 6th of October City 12568, Egypt

⁴Department of Mechanical and Aerospace Engineering, Politecnico di Torino, Torino 10129, Italy

⁵Università di Torino, Torino 10124, Italy

⁶Department of Oncology, Cross Cancer Institute, University of Alberta, Edmonton, AB T6G 1Z2, Canada

⁷Faculty of Pharmacy and Pharmaceutical Sciences, University of Alberta, Edmonton, AB T6G 2H1, Canada

This article has been accepted for publication and undergone full peer review but has not been through the copyediting, typesetting, pagination and proofreading process, which may lead to differences between this version and the [Version of Record](#). Please cite this article as [doi: 10.1111/CBDD.13660](https://doi.org/10.1111/CBDD.13660)

This article is protected by copyright. All rights reserved

⁸Cancer Research Institute of Northern Alberta, University of Alberta, Edmonton, AB T6G 2E1, Canada

¹Current address: Vancouver Prostate Centre, University of British Columbia, Vancouver, BC V6H 3Z6, Canada

[#]These authors contributed equally to this work

^{*}Correspondence: jackt@ualberta.ca, tel. +1-780-964-4517

Acknowledgments

This work was supported by an Alberta Cancer Foundation Transformative Program (project 26603) awarded to MW, FGW and JAT. FG was supported by an Alberta Innovates graduate student scholarship and a Novartis Pharmaceuticals Canada Inc. graduate scholarship. AHM was supported by a Marshall Syska scholarship. Computer simulations were carried out using the Pharmamatrix cluster at the University of Alberta.

Conflict of interest

The authors declare no conflict of interest.

Abstract

The heterodimer of DNA excision repair protein ERCC-1 and DNA repair endonuclease XPF (ERCC1-XPF) is a 5'-3' structure-specific endonuclease essential for the nucleotide excision repair (NER) pathway, and it is also involved in other DNA repair pathways. In cancer cells, ERCC1-XPF plays a central role in repairing DNA damage induced by chemotherapeutics including platinum-based and crosslinking agents, thus its inhibition is a promising strategy to enhance the effect of these therapies. In this study, we rationally modified the structure of F06, a small molecule inhibitor of the ERCC1-XPF interaction (Jordheim et al., 2013), to improve its binding to the target. We followed a multi-step computational approach to investigate potential modification sites of F06, rationally design and rank a library of analogues, and identify candidates for chemical synthesis and *in vitro* testing.

Our top compound, **B5**, showed an improved half-maximum inhibitory concentration (IC_{50}) value of 0.49 μ M for the inhibition of ERCC1-XPF endonuclease activity, and lays the foundation for further testing and optimization. Also, the computational approach reported here can be used to develop DNA repair inhibitors targeting the ERCC1-XPF complex.

Keywords

Computer-aided drug design, molecular dynamics, virtual screening, DNA repair, ERCC1-XPF, small molecules, protein-protein interaction, chemotherapy

Introduction

Genomic instability is associated with the aging process (López-Otín, Blasco, Partridge, Serrano, & Kroemer, 2013) and it is an enabling characteristic to acquire the hallmarks of cancer (Hanahan & Weinberg, 2011). Therefore, it is not surprising that cells require a well-functioning DNA repair apparatus to be protected from endogenous and exogenous damaging agents and to preserve their healthy status. Likewise, defective DNA repair pathways are associated with rare genetic diseases, such as xeroderma pigmentosum, Cockayne's syndrome and trichothiodystrophy, whose affected individuals show propensity for cancer, neurological deficiencies and physical abnormalities (Bukowska & Karwowski, 2018; Cleaver, Lam, & Revet, 2009). Although DNA repair is essential to maintain genomic stability, these pathways can interfere with cancer therapies by repairing the damage inflicted on tumor cells, allowing cancer to progress. Combination cancer therapy is a relatively new strategy in which a DNA-damaging agent (e.g. cisplatin) and a DNA repair inhibitor are jointly administered to the patient in order to potentiate the effect of the former (Helleday, Petermann, Lundin, Hodgson, & Sharma, 2008). The therapeutic potential of DNA repair inhibitors was recently demonstrated by the successful development of inhibitors for poly(ADP-ribose) polymerase (PARP) enzymes, with several molecules that either were approved for clinical use or entered clinical trials (Ohmoto & Yachida, 2017). Despite the increasing interest in DNA repair proteins as potential drug targets, there are very few known inhibitors besides the aforementioned PARP inhibitors. In particular, there are a number of other, complementary DNA repair mechanisms that could be exploited for anti-cancer therapy (Brown, O'Carrigan, Jackson, & Yap, 2017).

The heterodimeric protein ERCC1-XPF, made up of the DNA excision repair protein ERCC1 and the DNA repair endonuclease XPF, is a 5'-3' structure-specific endonuclease which cleaves double-strand/single-strand DNA junctions (McNeil & Melton, 2012). The catalytic activity of ERCC1-XPF is essential for the nucleotide excision repair (NER) pathway in order to repair bulky, helix-distorting damages such as UV-induced cyclobutane pyrimidine dimers, and is also involved in the repair of double-strand breaks (DSBs) and inter-strand crosslinks (ICLs) (Faridounnia, Folkers, & Boelens, 2018) (see Figure 1). NER and ICL repair are the main mechanisms responsible for removing damage induced by platinum-based and other crosslinking chemotherapy. Inhibiting these processes sensitize cancer cells to chemotherapy (Arora, Kothandapani, Tillison, Kalman-Maltese, & Patrick, 2010; McNeil & Melton, 2012; Mendoza et al., 2013), hence ERCC1-XPF is an attractive target for developing DNA repair inhibitors (McNeil & Melton, 2012).

Due to its central role in mediating therapeutic damage inflicted to cancer cells, ERCC1-XPF has been the subject of a number of studies aimed at developing DNA repair inhibitors (Gentile, A. Tuszynski, & H. Barakat, 2016). A first line of research was devoted to the discovery of inhibitors of the NER-specific interaction between the DNA repair protein complementing XP-A cells (XPA) and ERCC1 (Barakat et al., 2012; Gentile, Tuszynski, & Barakat, 2016). ERCC1-XPF is recruited to the damaged zone through this interaction in NER, and XPA-ERCC1 inhibitors showed promising preclinical potential to enhance the effect of cisplatin on tumors, although this approach would be effective on NER only without affecting other ERCC1-XPF-mediated pathways that do not involve XPA (Barakat et al., 2012). The catalytic site of the endonuclease has been explored as a target for inhibition as well. The site is on the XPF nuclease domain and contains a number of charged residues and metal ions, which make it an attractive target for small molecule binding. Recently, several inhibitors have been reported, some of which have been shown to enhance chemotherapy in cell and xenograft tumor models (Arora et al., 2016; Chapman, Gillen, et al., 2015; Chapman, Wallace, et al., 2015; Gentile, Barakat, & Tuszynski, 2018; McNeil et al., 2015). However, the similarity between catalytic sites of several human divalent cation-based DNA-cleaving enzymes constitutes an obstacle to designing XPF-specific inhibitors, and an experimental structure of the human XPF nuclease domain has not been solved yet (McNeil & Melton, 2012). Lastly, the ERCC1-XPF protein-protein interaction represents another interesting target for pharmacological inhibition since dimerization is

required to generate a functional endonuclease. Despite the high-affinity, hydrophobic-driven interaction between the double helix-hairpin-helix (HhH2) domains of ERCC1 and XPF, the interaction is specific to ERCC1-XPF and the deletion of a single residue (F293) at the ERCC1 side is enough to abrogate dimerization and nuclease activity. These characteristics make the ERCC1-XPF dimerization interface a promising, yet challenging, drug target for DNA repair inhibition (McNeil & Melton, 2012).

Some of us previously reported F06, the first ERCC1-XPF dimerization inhibitor, which binds at the XPF pocket interacting with ERCC1's F293, disrupts the protein-protein interaction, selectively blocks ERCC1-XPF-mediated DNA repair, and sensitizes cancer cell lines to UV and DNA-damaging drugs such as cisplatin and mitomycin C (Jordheim et al., 2013). More recently, we successfully combined computer-aided drug design (CADD) with a structure-activity relationship approach to extend the piperazine ring of F06 with different substituents, in order to improve the biological activity of this class of compounds. In this way we assessed F06 as a suitable scaffold for developing DNA repair inhibitor drug candidates (Elmenoufy et al., 2019). Building on our previous results, we report a new CADD strategy for further improvement of F06, which uses molecular dynamics (MD) to characterize in detail the structural changes introduced by F06 binding to XPF compared to XPF free form and ERCC1-XPF heterodimer. We also evaluated the hydrogen bond network of F06 with XPF in order to design F06 analogues with enhanced protein interaction patterns. In contrast to our earlier study where we modified a solvent-exposed group of F06 (Elmenoufy et al., 2019), here we focused on different modifications such as truncation of the lateral branch of F06 and substitution of the methoxy group with hydrogen bond acceptor groups to improve buried ligand-receptor interactions. Through our CADD-driven medicinal chemistry strategy, we developed **B5**, an analogue showing 3-fold increased inhibition of the ERCC1-XPF incision activity *in vitro*. Our results confirm F06 as a suitable scaffold for designing DNA repair inhibitors, and propose a rational approach to improve the affinity of the compounds to the target.

Methods

Molecular dynamics of XPF HhH2 domain alone, F06-bound and ERCC1-bound

We computationally predicted F06 as binding to a pocket of the HhH2 domain of XPF, replacing the side chain of F293 from ERCC1 in the dimer (Jordheim et al., 2013). Using classical MD simulations, we compared the unbound, F06-bound and ERCC1-bound form of the HhH2 domain of XPF (residues 822 to 905). For the F06-XPF complex, we used the structure previously obtained from docking simulations (Elmenoufy et al., 2019). The unbound and ERCC1-bound forms were extracted from the NMR ensemble of ERCC1-XPF dimerized HhH2 domains (PDB 1Z00) (Tripsianes et al., 2005), where the bound ERCC1 structure was excluded and included in the simulation, respectively.

The protonation states of the systems were assigned using the H++ server by setting pH=7, a salinity of 0.15 M, a dielectric constant of 10 for the solute and a solvent dielectric constant of 80 as input parameters (Anandakrishnan, Aguilar, & Onufriev, 2012). In AmberTools14 tleap (Case et al., 2015), we assigned Amber ff14SB force field parameters to the proteins (Maier et al., 2015), and the 12-6-4 parameters for mono- and divalent ions in TIP3P water to the ions as previously recommended (Li, Roberts, Chakravorty, & Merz, 2013; Li, Song, & Merz, 2015). We assigned the parameters of the Generalized Amber Force Field (GAFF) (Wang, Wolf, Caldwell, Kollman, & Case, 2004) and AM1-BCC charges (Jakalian, Jack, & Bayly, 2002) to F06 using Antechamber (Wang, Wang, Kollmann, & Case, 2005). The three systems were solvated with octahedral boxes of TIP3P explicit water molecules (Jorgensen, Chandrasekhar, Madura, Impey, & Klein, 1983) with 15 Å of buffer. The required numbers of Na⁺ and Cl⁻ ions were added to neutralize the overall charge of the system and establish a 0.15 M physiological ionic concentration. We then ran MD simulations of the systems using pmemd.cuda (Salomon-Ferrer, Götz, Poole, Le Grand, & Walker, 2013) with the following procedure: relaxation of ions and water molecules through 1000 steps of steepest descent and 1000 steps of conjugate gradient minimization, keeping protein and ligand atoms harmonically restrained with a force constant of 500 kcal/mol/Å². 2000 steps of steepest descent, followed by 3000 conjugate gradient steps without any restraint. Gradual heating from 0 to 300 K over 100 ps using the Langevin thermostat, keeping the backbone and ligand heavy atoms harmonically restrained (2 kcal/mol/Å²), and using a time step of 0.5 fs and NVT conditions. Gradual release of the restraints in four NPT phases of 50 ps where the force constant was reduced by 0.5 kcal/mol/Å² at each phase, with a time step of 2 fs. 250 ns of NPT production simulation with a time step of 2 fs. The cut-off for long-range interactions was set to 9 Å.

After the simulations, we calculated the mass-weighted root-mean square deviation (RMSD) of the heavy atoms of protein backbone and ligand using cpptraj from AmberTools14. We also carried out a secondary structure analysis over the MD trajectories using the dictionary of protein secondary structure (DSSP) method from cpptraj (Kabsch & Sander, 1983).

Analysis of the binding mode of F06

In order to investigate the dynamics of the F06-XPF interactions, we analyzed the hydrogen bonds occurring between F06 and the receptor and F06 and solvent, respectively, during the equilibrated part of the MD trajectory, using cpptraj. We defined as hydrogen bonds non-bonded interactions occurring between donor-hydrogen and acceptor atoms, which deviated no more than 60° from linearity and with a maximum distance of 3.5 Å between the two heavy atoms.

Using the MOE (Molecular Operating Environment) Pharmacophore Query Editor and the EHT scheme, we generated a set of essential pharmacophore features of F06, based on the docking pose of the compound (Lin, 2004). Electrostatic maps of the binding site were generated as reported previously (Elmenoufy et al., 2019).

Computer-aided design of F06 analogues

As a starting point for our computer-aided generation of analogues, we used the previously obtained docking pose of F06. We created an extensive, non-redundant collection of multi-conformational fragments by merging the MOE Linker library (Chemical Computing Group Inc., 2015), the ChEMBL fragment database (Chemical Computing Group Inc., 2015), the Cambridge Structure Linker database (Groom, Bruno, Lightfoot, & Ward, 2016), and a collection of fragments derived from the ZINC15 3D database (Sterling & Irwin, 2015). This last library was generated using the MOE2015 SD Pipelining Command tools (Chemical Computing Group Inc., 2015) to obtain different protonation states and tautomers, remove non-lead-like, reactive and large-ring structures, and generate molecular fragments. Up to five conformations for each ZINC15-derived fragment were obtained using Conformation Import and imposing a strain limit of 4 kcal/mol. We then used the collection of fragments for MOE2015 Scaffold Replacement (Chemical Computing Group Inc., 2015) of F06 substructures. We also used the MOE MedChem transformation tool (175 modification rules)

(Chemical Computing Group Inc., 2015) on the same F06 groups, with 6 iterations and a protein-ligand clash energy limit of 0.5 kcal/mol/ligand atom. For both Scaffold Replacement and MedChem transformations, we ran minimization of the resulting poses with protein side chains free to move and generalized Born Volume Integral/Weighted Surface Area (GBVI/WSA) function for scoring (Labute, 2008).

Structure-based virtual screening

In order to rank the analogues generated in the previous step, we adopted the same structure-based virtual screening (VS) strategy that we successfully used before (Elmenoufy et al., 2019). Molecular docking simulations were run with MOE Dock (Chemical Computing Group Inc., 2015). The pharmacophore model was used for the placement step, in which 30 high-scoring poses were returned, based on the London dG scores (Labute, 2008). Poses were minimized together with the side chains of the binding site (Induced Fit), and one pose was returned as the top-scored by the GBVI/WSA scoring function. We calculated logP values of the molecules using the SlogP function in MOE (Wildman & Crippen, 1999), as well as docking ligand efficiencies (final score/number of ligand heavy atoms).

We ran MD simulations of the top 200 analogue-XPF complexes resulting from docking. The systems were prepared in the same way as the F06-XPF system, and simulation setups were the same except for the length of the production simulations (2 ns). For MD snapshots extracted every 10 ps from the production simulations, we calculated the enthalpic portion of the binding energy using the Molecular Mechanics/Generalized Born Surface Area (MM/GBSA) method (Onufriev, Bashford, & Case, 2004) implemented in the MMPBSA.py script (Miller et al., 2012). In MM/GBSA, the free energy change due to ligand binding is calculated as

$$\Delta G_{bind, solv} = \Delta G_{MM, vac} + \Delta G_{solv, complex} - (\Delta G_{solv, ligand} + \Delta G_{solv, protein}) - T\Delta S \quad (\text{Eq. 1})$$

where $\Delta G_{MM, vac}$ includes averaged non-bonded molecular mechanics terms (electrostatic and van der Waals) occurring between protein and ligand. Solvation terms are modeled as

$$\Delta G_{solv} = \Delta G_{solv, polar} + \Delta G_{solv, npolar} \quad (\text{Eq. 2})$$

where the polar contribution of the solvent is calculated by the Generalized Born equation (Genheden & Ryde, 2015). Here, we used the GB^{OCBII} model and the modified radii from Onufriev et al. (Onufriev et al., 2004), and an ionic concentration of 0.15 M. The hydrophobic contribution to the solvation free energy is calculated as

$$\Delta G_{solv, npolar} = \gamma \cdot SASA \quad (\text{Eq. 3})$$

with γ (surface tension) as 0.005 kcal/mol/Å², and the solvent-accessible surface area (*SASA*) calculated using the linear combinations of pairwise overlaps (LCPO) model method (Weiser, Shenkin, & Still, 1999). Averaged values were estimated for the ligand-receptor (LR) complex, receptor (R) and ligand (L) alone, and final values were calculated as a difference between these three values (LR-R-L).

The entropy change is represented in the free energy equation by the $T\Delta S$ term. S was calculated for each trajectory by using the Amber normal mode analysis (NMA) method for the LR, R and L systems and then calculating the difference between the three systems (Kassem, Ahmed, El-Sheikh, & Barakat, 2015). Pairwise decomposition of binding energies was also carried out for the top compounds and the residues of the XPF pocket.

Preparation of F06-based analogues (Gen B compounds)

General synthesis of final Gen **B** compounds was achieved through a nucleophilic substitution reaction of the Gen **B1** (2-hydroxy 6,9 chloroacridine) and acyl chloride or chloride substituted derivatives to afford compounds Gen **B3** and Gen **B4**, respectively. Synthesis of Gen **B1** was achieved through dealkylation of 2-methoxy 6,9 chloroacrdine using BBr₃ in dichloromethane under nitrogen for 8 hours at room temperature. Syntheses of F06, Gen **B2** and Gen **B5** were performed according to our reported procedure (Elmenoufy et al., 2019) with minor modifications, which was through a one pot three sequential addition reaction; Mannich reaction of *p*-acetamidophenol with formaldehyde and appropriate secondary amine in 2-propanol was carried out under reflux for 12 h. The solvent and excess of the unreacted formaldehyde from the resulting mixture were removed under vacuum and, without isolating the compound, the resulting viscous residue was treated with 6 M HCl

to deacetylate the acetamido group to furnish the primary amine. Afterwards, an equimolar amount of 2-methoxy 6,9 chloroacridine or 2-hydroxy 6,9 chloroacridine was added, affording after heating compounds F06 or Gen **B2** and Gen **B5** respectively in moderate to good yields after isolation. The synthesis is general, facile and reproducible. The high-performance liquid chromatography (HPLC) analyses were performed using an Agilent 1100 LC/MSD instrument. Elution was done with a gradient of 10–95% solvent B in solvent A (solvent A was 0.1% TFA in water, and solvent B was 0.1% acetic acid in MeCN) through an Agilent column eclipse XDB- C18 (4.6 × 250 mm, 5 μm) column at 1.0 mL/min. Area % purity was measured at 210 and 254 nm. The purity of the most active compound Gen **B5** was assessed by HPLC (>98% purity). All synthesized compounds were characterized by ¹H NMR, ¹³C NMR, HRMS, IR and the purity of most active compound **B5** was determined by HPLC.

ERCC1-XPF protein preparation

Human ERCC1-XPF wild-type proteins were obtained as previously described (Bowles et al., 2012; Elmenoufy et al., 2019).

Microplate fluorescence incision assay

ERCC1-XPF incision was measured in a microplate incision assay as previously described (Bowles et al., 2012; Elmenoufy et al., 2019).

Results and discussion

Molecular dynamics simulations

The MD simulation of the unbound form of XPF revealed a dramatic change from the initial structure extracted from the complex with ERCC1, with ~8 Å of difference in RMSD (shown in red in Figure 2a) from the ERCC1-bound form (shown in green in Figure 2a). Remarkably, despite the small size of F06 compared to the ERCC1 HhH2 domain, the binding of the ligand to the XPF pocket (which hosts ERCC1's F293 in the heterodimer) led to a stable XPF conformation which diverged from the ERCC1-bound equilibrated structure by only ~2 Å in terms of RMSD (shown in blue in Figure 2a).

MD results suggest that the binding of F06 to the F293 hotspot-interacting pocket on XPF (de Laat, Sijbers, Odijk, Jaspers, & Hoeijmakers, 1998; McNeil & Melton, 2012; Sijbers et al., 1996; Tripsianes et al., 2005) can substitute for ERCC1 as a binding partner of XPF and induce an conformation close to the ERCC1-bound one. The RMSD of the heavy atoms of F06 during the production MD simulation fluctuated around an average value of 1 Å from the starting conformation, indicating a stable pose of the ligand within the binding site of XPF (Figure 2b).

To assess further the structural differences between the three XPF models, we extracted and superposed the lowest potential energy structures of XPF from the MD trajectories. The ERCC1-bound (shown in green in Figure 3a) and F06-bound (shown in blue in Figure 3a) form showed a similar tertiary structure, suggesting again that F06 may mimic the natural ERCC1 partner and cause subsequently a similar conformation of XPF to be present. The unbound XPF (shown in red in Figure 3a) showed a less ordered conformation compared to the other two structures. The main structural change observable in the unbound form was the loss of the HhH2 typical domain structure and the disruption of the H1 alpha helix (residue 834-845) (Figure 3b), as revealed also by the DSSP analysis performed over the last 100 ns of MD simulation (Figure 3c). Importantly, H1 is part of the F06 binding site. Overall, the ERCC1-bound and the F06-bound structures showed more globular shapes compared to the unbound form, with less exposure of the hydrophobic regions devoted to interact with ERCC1, in agreement with previous experimental observations (McNeil & Melton, 2012; Tripsianes et al., 2005).

Interactions of F06 with the XPF binding site

In our earlier work (Elmenoufy et al., 2019) we synthesized and tested analogues generated by modifying an hydrophobic, solvent-exposed moiety of F06. In the present work, we focused on polar groups of F06. We carried out hydrogen bond analysis of the last 100 ns of the XPF-F06 trajectory, in order to assess polar interactions established by the ligand with the receptor and solvent molecules (Table 1). The charge-assisted hydrogen bond between the N2-H atoms of F06 (Figure 4) and the negatively charged side chain of E831 of XPF was the most prevalent interaction, present in 37% of the last 100 ns of the MD trajectory. N3 of F06 also established hydrogen bond interactions with the backbone atoms of V859 and M856 for 26% of the equilibrated trajectory. N4 was the main hydrogen

bond acceptor atom of F06, establishing a hydrogen bond with N834 of XPF for 9% of the 100 ns (Table 1). These three interactions showed also good hydrogen bond average geometries in terms of distances (2.88 – 3.10 Å) and angles (~160°) (Schaeffer, 2015). The other polar moieties of F06 were involved in hydrogen bonds with solvent molecules during the simulation, rather than specific interactions with XPF (Table 1). Interestingly, O2 of F06 was the only polar atom not involved in any hydrogen bond with XPF, despite its buried position and both acceptor and donor-favourable interaction spots present around it (Figure S1 in Supplementary Material).

Virtual screening of F06 analogues

We generated a virtual library of analogues by modifying two groups of F06 (Figure 5), namely 1) the methoxy group of site 1, in order to establish an additional favourable hydrogen bond; and 2) the lateral branch of the acridine scaffold of F06 to reduce the solvent-exposed portion of the compound (site 2). We also included the piperazine ring extension of compound 4, the most active F06 analogue identified in the previous medicinal chemistry campaign (Elmenoufy et al., 2019).

The resulting library includes 5650 structures. Because different features were introduced in the analogues, we defined an essential pharmacophore model based on the conserved acridine core, with three aromatic features accounting for the aromatic rings anchoring the compounds to the hydrophobic floor of the binding site (Figure S2 in Supplementary Material), and we used it for pharmacophore-assisted docking in MOE, followed by MD-MM/GBSA-based rescoring. Among the top ranked virtual hits, we selected 5 compounds for synthesis based on visual inspection of their poses, MM/GBSA scores, and synthetic chemistry feasibility. These compounds (Figure 6) were synthesized successfully and their activities were validated with a cell-free assay of ERCC1-XPF incision activity (discussed below). Gen **B1** was a truncated version of F06 with the hydroxy acridine rather than methoxy group branched out of the acridine. Gen **B2** was a more complete analogue of F06 but with the hydroxy group replacing the methoxy group. Gen **B3** and **B4** were functionalized to have phenyl groups tethered with ester or ether linkage, respectively, at site 1. Gen **B5** was composed of N-methyl piperazine extension at site 1 and the hydroxy acridine at site 2. Binding energies and other computationally derived values for F06 and the series of analogues are reported in Table 2.

Inhibition of ERCC1-XPF DNA incision activity by F06 analogues

In order to assess the ability of the F06 analogues to inhibit ERCC1-XPF, we used an *in vitro* real-time fluorescence-based incision assay that we previously developed (Elmenoufy et al., 2019). In this assay, the activity of ERCC1-XPF results from an increase of time-dependent fluorescent signal caused by the release of a fluorescent 8-base DNA fragment upon cleavage (Figure 7). Compared with the absence of compounds, a lower initial velocity of the reaction (V_0 , signal curve slope) is expected when an ERCC1-XPF inhibitor is present. Two analogues showed increased activity when compared to F06, namely compound **B2** and **B5**. In particular, **B5** was the best inhibitor of this generation of analogues, and the second-highest scored structure from VS; the calculated logP value for **B5** (2.31) was also the lowest observed between all the F06 analogues we have investigated so far (Elmenoufy et al., 2019). Different concentrations of **B5** ranging from 0 to 10 μM were plotted against the velocities in presence of the inhibitor at such concentrations, and half-maximum inhibitory concentration (IC_{50}) was estimated as $0.49 \pm 0.04 \mu\text{M}$, while IC_{50} of F06 was $1.86 \pm 0.25 \mu\text{M}$ (Elmenoufy et al., 2019). The improved inhibitory activities of **B2** and **B5** suggest the replacement of the methoxy group with a hydrogen bond donor group together with the conservation or extension of the piperazine ring as a viable strategy for further improving the F06 structure. Interestingly, the modest values of binding energies calculated computationally for **B1** were compensated by a very satisfactory ligand efficiency ($-0.31 \text{ kcal/mol/heavy atom}$) and an inhibitory activity was observed in the assay, suggesting that this analogue could be considered for further investigations due to its small size and the absence of the lateral branch exposed to solvent in F06.

Since **B5** was the most active analogue of the series, we carried out a detailed analysis of its predicted binding pose based on the 2 ns-long MD simulation and MM-GBSA calculations, and compared it with the analysis for F06. The lowest potential energy conformation of the XPF-**B5** complex extracted from the 2 ns MD simulation (Figure 8a) showed a hydrophobic stacking of the acridine moiety of **B5** between the side chains of Y833 and K860 of F06 (Figure 8a and b), resulting in more favourable contributions to the overall binding affinity by these residues compared to XPF-F06 (Figure 8c). N834 was involved in a hydrogen bond with **B5**, similarly to F06 (Figure 8a and b). The hydroxyl group substituting the methoxy in **B5** was involved in a new hydrogen bond established with the side

chain of V859, not observed for F06 or our previous compound 4 (Elmenoufy et al., 2019). Consistent with our previous observations, the acridine moiety was buried inside the XPF pocket while the piperazine ring extension derived from compound 4 resulted in enhanced interactions with the solvent and E829 (Figure 8b), although the latter was less strong than the one observed for F06 (Figure 8c).

Conclusions

Interest is growing in the role of the ERCC1-XPF endonuclease as a drug target in cancer treatment, due to its critical role in repairing DNA damage inflicted by platinum-based and cross-linking chemotherapy. Abnormal regulation of levels of XPF, ERCC1 or related proteins has been linked with modulation of the response to DNA-damaging treatments, either showing resistance in the case of over-regulation or sensitization in the case of down-regulation. Thus, ERCC1-XPF inhibition is a viable strategy to circumvent DNA damage-related drug resistance and improve the outcome of cancer therapy.

In this work we focused on designing small molecules able to disrupt the ERCC1-XPF protein-protein interaction, since heterodimerization of ERCC1 and XPF is required to constitute a functional complex (McNeil & Melton, 2012). We identified two compounds, **B2** and **B5**, with improved inhibition of the ERCC1-XPF incision activity compared to the parent compound F06. Compound **B1**, a truncated version of **B2** and **B5**, may also be a promising starting structure for further modifications due to its modest inhibitory activity despite the replacement of the bulky lateral branch of F06 with a chlorine.

To conclude, the workflow we introduced here provides a blueprint for future modification of other sites of F06 in order to develop preclinical drug candidates for DNA repair inhibition. Likewise, the set of analogues described in this study, especially **B1**, **B2** and **B5**, and their structure-activity relationships provide important information for the lead optimization process of F06. We plan to design a next generation of compounds aiming to further optimize the lead compound **B5**, which will be followed by more advanced *in vitro* and *in vivo* experimental testing.

Data availability statement

The data that support the findings of this study are available from the corresponding author upon reasonable request.

References

- Anandakrishnan, R., Aguilar, B., & Onufriev, A. V. (2012). H++ 3.0: automating pK prediction and the preparation of biomolecular structures for atomistic molecular modeling and simulations. *Nucleic Acids Research*, *40*(Web Server issue), W537-41. <https://doi.org/10.1093/nar/gks375>
- Arora, S., Heyza, J., Zhang, H., Kalman-Maltese, V., Tillison, K., Floyd, A. M., ... Patrick, S. M. (2016). Identification of small molecule inhibitors of ERCC1-XPF that inhibit DNA repair and potentiate cisplatin efficacy in cancer cells. *Oncotarget*, *7*(46), 75104–75117. <https://doi.org/10.18632/oncotarget.12072>
- Arora, S., Kothandapani, A., Tillison, K., Kalman-Maltese, V., & Patrick, S. M. (2010). Downregulation of XPF-ERCC1 enhances cisplatin efficacy in cancer cells. *DNA Repair*, *9*(7), 745–753. <https://doi.org/10.1016/j.dnarep.2010.03.010>
- Barakat, K. H., Jordheim, L. P., Perez-Pineiro, R., Wishart, D., Dumontet, C., & Tuszynski, J. A. (2012). Virtual screening and biological evaluation of inhibitors targeting the XPA-ERCC1 interaction. *PloS One*, *7*(12), e51329. <https://doi.org/10.1371/journal.pone.0051329>
- Bowles, M., Lally, J., Fadden, A. J., Mouilleron, S., Hammonds, T., & McDonald, N. Q. (2012). Fluorescence-based incision assay for human XPF-ERCC1 activity identifies important elements of DNA junction recognition. *Nucleic Acids Research*, *40*(13), e101. <https://doi.org/10.1093/nar/gks284>
- Brown, J. S., O’Carrigan, B., Jackson, S. P., & Yap, T. A. (2017). Targeting DNA Repair in Cancer: Beyond PARP Inhibitors. *Cancer Discovery*, *7*(1), 20–37. <https://doi.org/10.1158/2159-8290.CD-16-0860>
- Bukowska, B., & Karwowski, B. T. (2018). Actual state of knowledge in the field of diseases related with defective nucleotide excision repair. *Life Sciences*, *195*, 6–18.

<https://doi.org/10.1016/J.LFS.2017.12.035>

Case, D. ., Berryman, J. T., Betz, R. M., Cerutti, D. S., Cheatham III, T. E., Darden, T. A., ... Kollman, P. A. (2015). Amber 15. <https://doi.org/citeulike-article-id:2734527>

Chapman, T. M., Gillen, K. J., Wallace, C., Lee, M. T., Bakrania, P., Khurana, P., ... Saxty, B. (2015). Catechols and 3-hydroxypyridones as inhibitors of the DNA repair complex ERCC1-XPF. *Bioorganic & Medicinal Chemistry Letters*, 25(19), 4097–4103. <https://doi.org/10.1016/j.bmcl.2015.08.031>

Chapman, T. M., Wallace, C., Gillen, K. J., Bakrania, P., Khurana, P., Coombs, P. J., ... Saxty, B. (2015). N-Hydroxyimides and hydroxypyrimidinones as inhibitors of the DNA repair complex ERCC1-XPF. *Bioorganic & Medicinal Chemistry Letters*, 25(19), 4104–4108. <https://doi.org/10.1016/j.bmcl.2015.08.024>

Chemical Computing Group Inc. (2015). Molecular Operating Environment (MOE), 2015. Retrieved February 2, 2014, from <http://www.chemcomp.com>

Cleaver, J. E., Lam, E. T., & Revet, I. (2009). Disorders of nucleotide excision repair: the genetic and molecular basis of heterogeneity. *Nature Reviews Genetics*, 10(11), 756–768. <https://doi.org/10.1038/nrg2663>

de Laat, W. L., Sijbers, A. M., Odijk, H., Jaspers, N. G., & Hoeijmakers, J. H. (1998). Mapping of interaction domains between human repair proteins ERCC1 and XPF. *Nucleic Acids Research*, 26(18), 4146–4152. Retrieved from <http://www.ncbi.nlm.nih.gov/pubmed/9722633>

Elmenoufy, A. H., Gentile, F., Jay, D., Karimi-Busheri, F., Yang, X., Soueidan, O. M., ... West, F. G. (2019). Targeting DNA Repair in Tumor Cells via Inhibition of ERCC1-XPF. *Journal of Medicinal Chemistry*, 62(17), acs.jmedchem.9b00326. <https://doi.org/10.1021/acs.jmedchem.9b00326>

Faridounnia, M., Folkers, G. E., & Boelens, R. (2018, December 5). Function and interactions of ERCC1-XPF in DNA damage response. *Molecules*. Multidisciplinary Digital Publishing Institute.

<https://doi.org/10.3390/molecules23123205>

Genheden, S., & Ryde, U. (2015). The MM/PBSA and MM/GBSA methods to estimate ligand-binding affinities. *Expert Opinion on Drug Discovery*, 10(5), 449–461.

<https://doi.org/10.1517/17460441.2015.1032936>

Gentile, F., A. Tuszynski, J., & H. Barakat, K. (2016). Modelling DNA Repair Pathways: Recent Advances and Future Directions. *Current Pharmaceutical Design*, 22(23), 3527–3546.

<https://doi.org/10.2174/1381612822666160420141435>

Gentile, F., Barakat, K., & Tuszynski, J. (2018). Computational Characterization of Small Molecules Binding to the Human XPF Active Site and Virtual Screening to Identify Potential New DNA Repair Inhibitors Targeting the ERCC1-XPF Endonuclease. *International Journal of Molecular Sciences*, 19(5), 1328. <https://doi.org/10.3390/ijms19051328>

Gentile, F., Tuszynski, J. A., & Barakat, K. H. (2016). New design of nucleotide excision repair (NER) inhibitors for combination cancer therapy. *Journal of Molecular Graphics and Modelling*, 65(1), 71–82. <https://doi.org/10.1016/j.jmglm.2016.02.010>

Groom, C. R., Bruno, I. J., Lightfoot, M. P., & Ward, S. C. (2016). The Cambridge structural database. *Acta Crystallographica Section B: Structural Science, Crystal Engineering and Materials*, 72(2), 171–179. <https://doi.org/10.1107/S2052520616003954>

Hanahan, D., & Weinberg, R. A. (2011, March 4). Hallmarks of cancer: The next generation. *Cell*. Elsevier. <https://doi.org/10.1016/j.cell.2011.02.013>

Helleday, T., Petermann, E., Lundin, C., Hodgson, B., & Sharma, R. A. (2008). DNA repair pathways as targets for cancer therapy. *Nature Reviews. Cancer*, 8(3), 193–204.

<https://doi.org/10.1038/nrc2342>

Jakalian, A., Jack, D. B., & Bayly, C. I. (2002). Fast, efficient generation of high-quality atomic charges. AM1-BCC model: II. Parameterization and validation. *Journal of Computational Chemistry*, 23(16), 1623–1641. <https://doi.org/10.1002/jcc.10128>

Jordheim, L. P., Barakat, K. H., Heinrich-Balard, L., Matera, E.-L., Cros-Perrial, E., Bouledrak, K., ... Dumontet, C. (2013). Small molecule inhibitors of ERCC1-XPF protein-protein interaction synergize alkylating agents in cancer cells. *Molecular Pharmacology*, *84*(1), 12–24. <https://doi.org/10.1124/mol.112.082347>

Jorgensen, W. L., Chandrasekhar, J., Madura, J. D., Impey, R. W., & Klein, M. L. (1983). Comparison of simple potential functions for simulating liquid water. *The Journal of Chemical Physics*, *79*(2), 926. <https://doi.org/10.1063/1.445869>

Kabsch, W., & Sander, C. (1983). Dictionary of protein secondary structure: Pattern recognition of hydrogen-bonded and geometrical features. *Biopolymers*, *22*(12), 2577–2637. <https://doi.org/10.1002/bip.360221211>

Kassem, S., Ahmed, M., El-Sheikh, S., & Barakat, K. H. (2015). Entropy in bimolecular simulations: A comprehensive review of atomic fluctuations-based methods. *Journal of Molecular Graphics & Modelling*, *62*, 105–117. <https://doi.org/10.1016/j.jmkgm.2015.09.010>

Labute, P. (2008). The generalized Born/volume integral implicit solvent model: estimation of the free energy of hydration using London dispersion instead of atomic surface area. *Journal of Computational Chemistry*, *29*(10), 1693–1698. <https://doi.org/10.1002/jcc.20933>

Li, P., Roberts, B. P., Chakravorty, D. K., & Merz, K. M. (2013). Rational Design of Particle Mesh Ewald Compatible Lennard-Jones Parameters for +2 Metal Cations in Explicit Solvent. *Journal of Chemical Theory and Computation*, *9*(6), 2733–2748. <https://doi.org/10.1021/ct400146w>

Li, P., Song, L. F., & Merz, K. M. (2015). Systematic parameterization of monovalent ions employing the nonbonded model. *Journal of Chemical Theory and Computation*, *11*(4), 1645–1657. <https://doi.org/10.1021/ct500918t>

Lin, A. (2004). Overview of Pharmacophore Applications in MOE. Retrieved July 20, 2015, from <https://www.chemcomp.com/journal/ph4.htm>

López-Otín, C., Blasco, M. A., Partridge, L., Serrano, M., & Kroemer, G. (2013). The Hallmarks of

Aging. *Cell*, 153(6), 1194. <https://doi.org/10.1016/J.CELL.2013.05.039>

Maier, J. A., Martinez, C., Kasavajhala, K., Wickstrom, L., Hauser, K. E., & Simmerling, C. (2015). ff14SB: Improving the Accuracy of Protein Side Chain and Backbone Parameters from ff99SB. *Journal of Chemical Theory and Computation*, 11(8), 3696–3713. <https://doi.org/10.1021/acs.jctc.5b00255>

McNeil, E. M., Astell, K. R., Ritchie, A.-M., Shave, S., Houston, D. R., Bakrania, P., ... Melton, D. W. (2015). Inhibition of the ERCC1-XPF structure-specific endonuclease to overcome cancer chemoresistance. *DNA Repair*, 31, 19–28. <https://doi.org/10.1016/j.dnarep.2015.04.002>

McNeil, E. M., & Melton, D. W. (2012). DNA repair endonuclease ERCC1-XPF as a novel therapeutic target to overcome chemoresistance in cancer therapy. *Nucleic Acids Research*, 40(20), 9990–10004. <https://doi.org/10.1093/nar/gks818>

Mendoza, J., Martínez, J., Hernández, C., Pérez-Montiel, D., Castro, C., Fabián-Morales, E., ... Herrera, L. A. (2013). Association between ERCC1 and XPA expression and polymorphisms and the response to cisplatin in testicular germ cell tumours. *British Journal of Cancer*, 109(1), 68–75. <https://doi.org/10.1038/bjc.2013.303>

Miller, B. R., McGee, T. D., Swails, J. M., Homeyer, N., Gohlke, H., & Roitberg, A. E. (2012). MMPBSA.py : An Efficient Program for End-State Free Energy Calculations. *Journal of Chemical Theory and Computation*, 8(9), 3314–3321. <https://doi.org/10.1021/ct300418h>

Ohmoto, A., & Yachida, S. (2017). Current status of poly(ADP-ribose) polymerase inhibitors and future directions. *OncoTargets and Therapy*, 10, 5195–5208. <https://doi.org/10.2147/OTT.S139336>

Onufriev, A., Bashford, D., & Case, D. A. (2004). Exploring protein native states and large-scale conformational changes with a modified generalized born model. *Proteins*, 55(2), 383–394. <https://doi.org/10.1002/prot.20033>

Salomon-Ferrer, R., Götz, A. W., Poole, D., Le Grand, S., & Walker, R. C. (2013). Routine

Microsecond Molecular Dynamics Simulations with AMBER on GPUs. 2. Explicit Solvent Particle Mesh Ewald. *Journal of Chemical Theory and Computation*, 9(9), 3878–3888.
<https://doi.org/10.1021/ct400314y>

Schaeffer, L. (2015). The Role of Functional Groups in Drug-Receptor Interactions. In *The Practice of Medicinal Chemistry: Fourth Edition* (pp. 359–378). Academic Press.
<https://doi.org/10.1016/B978-0-12-417205-0.00014-6>

Sijbers, A. M., van der Spek, P. J., Odijk, H., van den Berg, J., van Duin, M., Westerveld, A., ... Hoeijmakers, J. H. (1996). Mutational analysis of the human nucleotide excision repair gene ERCC1. *Nucleic Acids Research*, 24(17), 3370–3380. Retrieved from
<http://www.ncbi.nlm.nih.gov/pubmed/8811092>

Sterling, T., & Irwin, J. J. (2015). ZINC 15 - Ligand Discovery for Everyone. *Journal of Chemical Information and Modeling*, 55(11), 2324–2337. <https://doi.org/10.1021/acs.jcim.5b00559>

Tripsianes, K., Folkers, G., Ab, E., Das, D., Odijk, H., Jaspers, N. G. J., ... Boelens, R. (2005). The structure of the human ERCC1/XPF interaction domains reveals a complementary role for the two proteins in nucleotide excision repair. *Structure*, 13(12), 1849–1858.
<https://doi.org/10.1016/j.str.2005.08.014>

Wang, J., Wang, W., Kollmann, P., & Case, D. (2005). Antechamber, An Accessory Software Package For Molecular Mechanical Calculation. *J. Comput. Chem.*, 25, 1157–1174.

Wang, J., Wolf, R. M., Caldwell, J. W., Kollman, P. A., & Case, D. A. (2004). Development and testing of a general amber force field. *Journal of Computational Chemistry*, 25(9), 1157–1174.
<https://doi.org/10.1002/jcc.20035>

Weiser, J., Shenkin, P. S., & Still, W. C. (1999). Approximate atomic surfaces from linear combinations of pairwise overlaps (LCPO). *Journal of Computational Chemistry*, 20(2), 217–230. [https://doi.org/10.1002/\(SICI\)1096-987X\(19990130\)20:2<217::AID-JCC4>3.0.CO;2-A](https://doi.org/10.1002/(SICI)1096-987X(19990130)20:2<217::AID-JCC4>3.0.CO;2-A)

Wildman, S. A., & Crippen, G. M. (1999). Prediction of physicochemical parameters by atomic

contributions. *Journal of Chemical Information and Computer Sciences*, 39(5), 868–873.

<https://doi.org/10.1021/ci9903071>

Tables

Table 1 Main ligand-receptor and ligand-solvent hydrogen bonds observed during the last 100 ns of MD simulation of the XPF-F06 complex. Only the bonds present in at least 5% of the trajectory are reported. Names of F06 polar atoms follow the scheme of Figure 4.

Donor	Acceptor	Ratio ^a	Average distance (Å)	Average angle (°)
F06@N2	E831	0.37	2.88	160.24
F06@N3	V859	0.15	2.98	159.68
F06@N3	M856	0.11	3.19	142.63
F06@N2	S830	0.08	2.98	140.18
F06@O1	Solvent ^b	0.92	2.78	160.81
F06@N3	Solvent ^b	0.75	3.02	160.20
F06@N2	Solvent ^b	0.68	2.95	155.90
N834	F06@N4	0.09	3.10	155.05
Solvent ^c	F06@N4	0.96	3.02	154.51
Solvent ^c	F06@N1	0.82	2.94	160.17
Solvent ^c	F06@CL1	0.49	3.28	138.81
Solvent ^c	F06@O1	0.41	3.07	148.57
Solvent ^c	F06@N3	0.13	3.24	145.08

^aRatio = (frames where the interaction was present)/(total number of frames)

^bWater, Na⁺ and Cl⁻

^cWater

Table 2 Computational results for the series of F06 analogues selected for chemical synthesis. The list is in ascending order based on MM/GBSA scores.

Compound	GBVI/WSA ^a (kcal/mol)	Ligand efficiency ^b (kcal/mol/ha)	MM/GBSA (kcal/mol)	LogP
----------	-------------------------------------	---	-----------------------	------

F06	-6.70	-0.20	-17.78	4.10
B3	-8.56	-0.21	-14.19	5.31
B5	-7.00	-0.19	-12.44	2.31
B4	-5.17	-0.13	-8.15	5.93
B1	-5.21	-0.31	-7.11	4.40
B2	-5.90	-0.18	-3.79	3.79

^aFrom MOE Dock

^bDocking binding energy/heavy atoms (ha)

Figure legends

Figure 1 The ERCC1-XPF complex is involved in three major DNA repair pathways: a) in NER, adduct-caused distortions of the double helix are detected and the double stranded filament is opened and stabilized by the repair machinery; ERCC1-XPF and XPG endonucleases are then recruited at 5' and 3', respectively, for the cleavage and removal of the single-strand lesion. The free 3'-OH terminal is then used as a primer for the synthesis of the missing fragment. b) ICLs seriously hinder the replication machinery, eventually leading to formation of double-strand breaks. ERCC1-XPF is involved in the incision either side of an ICL from one strand allowing the passage of polymerases and the filling of the gaps. c) In DSB repair pathway the damaged DNA can be fixed either by homologous recombination or microhomology-mediated end joining. Independently of the repair mechanism, ERCC1-XPF is needed to remove 3' single strand flaps formed by non-homologous fragments at the edges of the former break, to allow ligases to seal gaps and restore the integrity of the double helix.

Figure 2 a) RMSDs of backbone atoms of unbound (red), F06-bound (blue) and ERCC1-bound XPF (green) from MD simulations. The initial structure was the same in all three cases, i.e., the XPF conformation bound to ERCC1. The systems reached a RMSD plateau after ~150 ns of simulation in explicit solvent. Binding of F06, despite the reduced size of the ligand compared to the ERCC1 HhH2 domain, partially restored the RMSD trend to the ERCC1-bound form, indicating a stabilizing effect upon binding to the pocket of XPF, and suggesting F06 as a dimerization inhibitor able to replace

ERCC1 as a binding partner. b) RMSD of F06 heavy atoms. The ligand kept a stable pose within the binding pocket of XPF, with an average displacement of ~ 1 Å from the starting structure.

Figure 3 Structural differences between bound and unbound forms of XPF. a) ERCC1-bound (green) and F06-bound (blue) displayed a similar tertiary structure of the domain, with a well-formed HhH2 domain, despite the difference in size and interaction interface between ERCC1 and F06. The unbound form (red) lost the HhH2 structure and adopted a less globular conformation. b) Residues constituting H1 (in yellow) showed an alpha helical structure in the two bound forms, while a more disordered structure was observed in the unbound form. H1 is part of the binding site of F06. c) DSSP analysis of H1 residues in the last 50000 frames (100 ns) of MD simulations, confirming the prevalence of alpha helical conformations for the XPF bound forms, differently from the unbound form.

Figure 4 Protonated 3D structure of F06. Polar atoms are labelled with their names.

Figure 5 Modification sites of F06 explored using a CADD strategy. The choice of sites was driven by the analysis of the binding pose of the original compound F06.

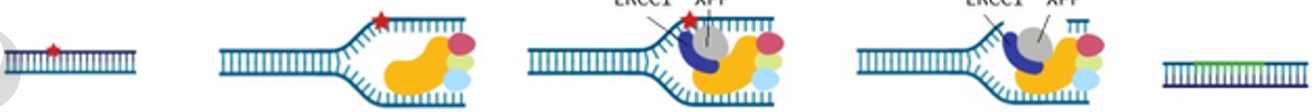
Figure 6 VS-derived compounds selected for chemical synthesis, exploring a variety of modifications of site 1 and 2 of F06.

Figure 7 Representative plot of the change of fluorescence versus time. Increase of relative fluorescence units (RFU) is due to the release of a fluorescent 8-base fragment and indicates ERCC1-XPF-mediated DNA cleavage. Control refers to ERCC1-XPF activity in the presence of carrier but not inhibitor.

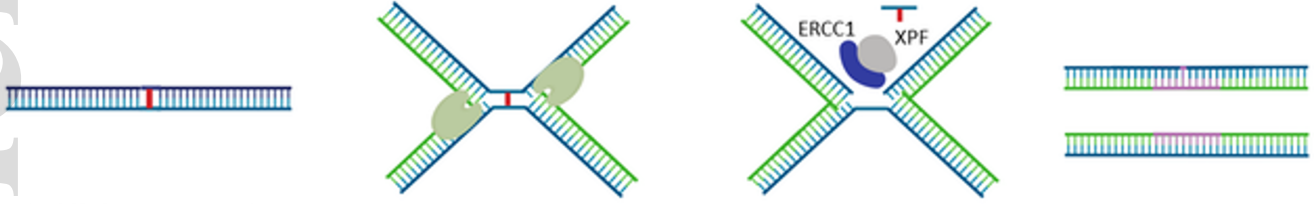
Figure 8 Detailed analysis of the predicted binding mode of **B5** to XPF derived from the 2 ns-long MD simulation. a) lowest potential energy XPF (white and green) - **B5** (yellow) conformation extracted from the simulation. The acridine moiety was stacked between the side chains of Y833 and K860. Hydrogen bonds between **B5** and N834 and V859 were observed. b) Ligand interaction diagram of the lowest potential energy conformation; the lateral branch of **B5** containing the piperazine ring extension was solvent-exposed (blue clouds) thanks to its polar and charged groups

that favourably interacted with the surrounding water molecules. c) Per-residue decomposition of the total MM/GBSA binding energy of **B5** (blue) and F06 (orange).

a) NER pathway



b) ICL repair pathway

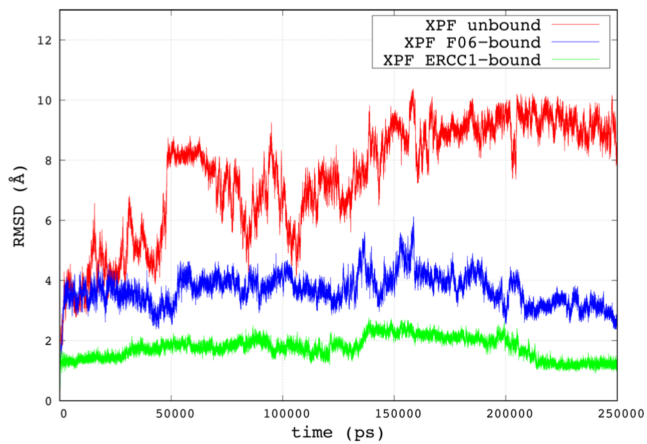


c) DSB repair pathway

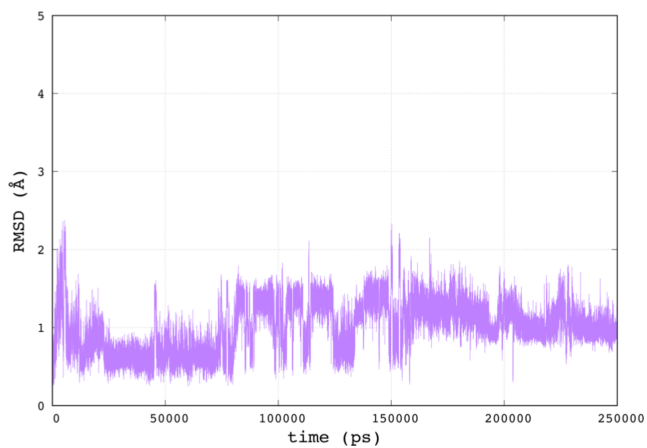


cbdd_13660_f1.tif

a)

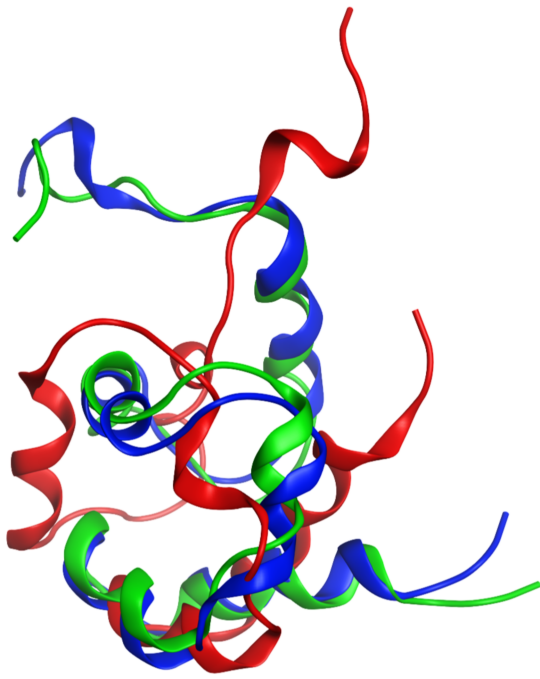


b)

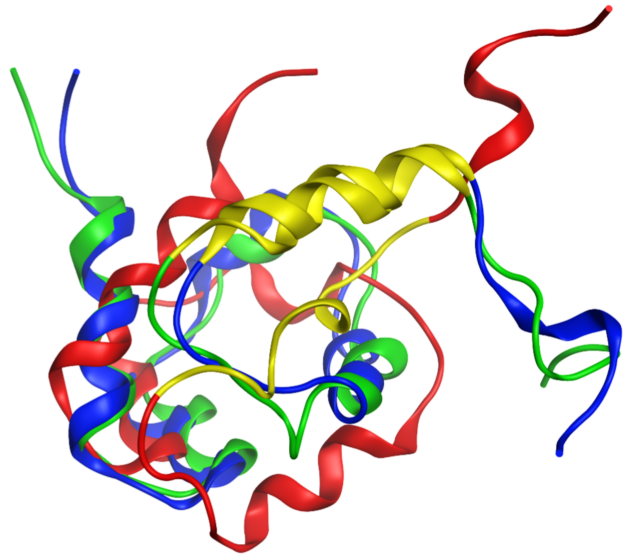


cbdd_13660_f2.tif

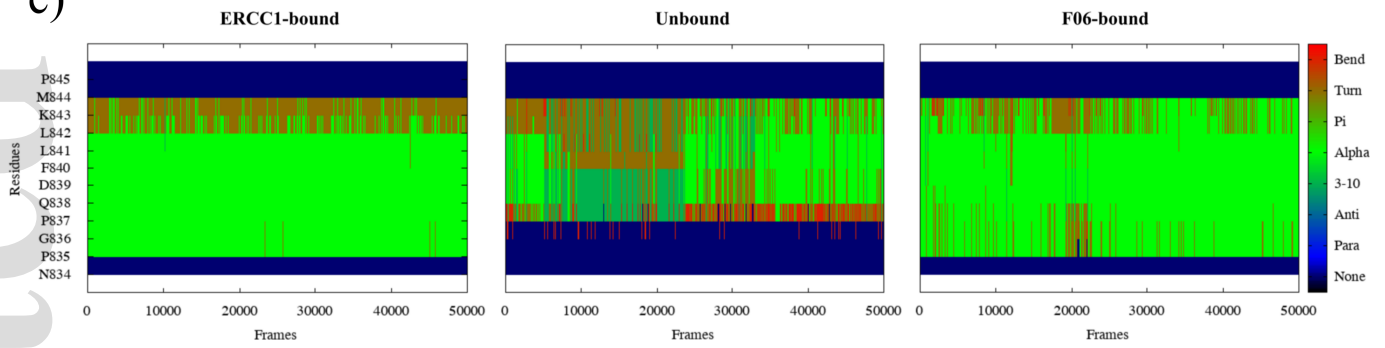
a)

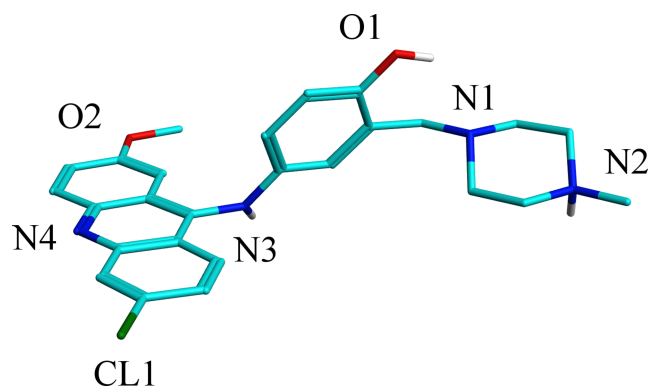


b)

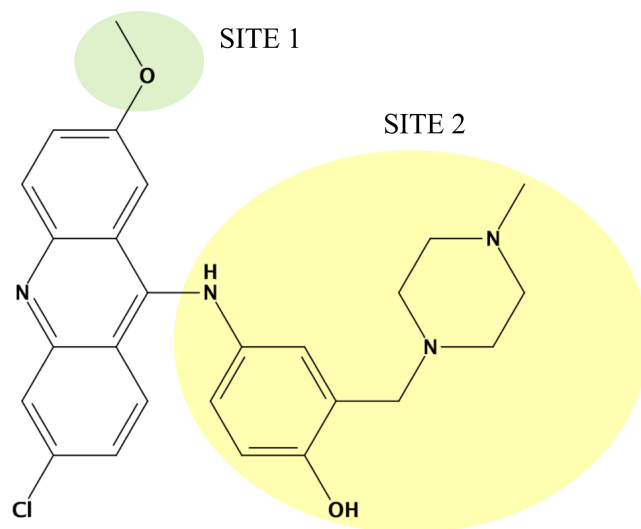


c)

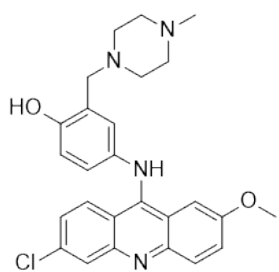




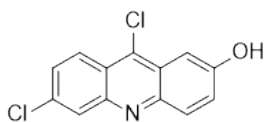
cbdd_13660_f4.tif



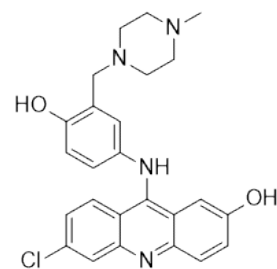
cbdd_13660_f5.tif



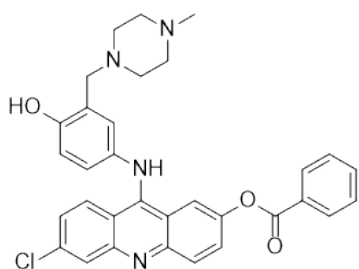
F06



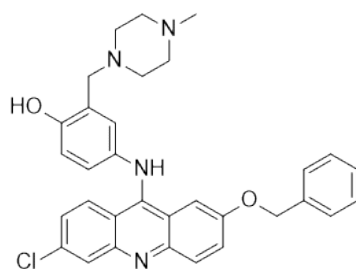
B1



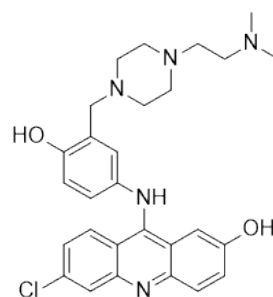
B2



B3

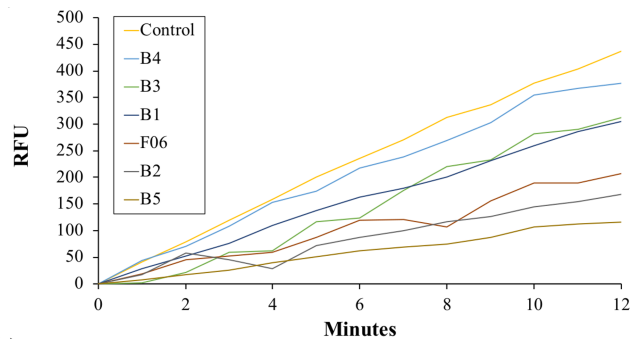


B4



B5

cbdd_13660_f6.tif



cbdd_13660_f7.tif

